J Mater Sci (2011) 46:6988–6997
DOI 10.1007/s10853-011-5667-5

Kinetic studies on water-soluble gold nanoparticles coordinated to poly(vinylpyrrolidone): isotropic to anisotropic transformation and morphology

Md. Habib Ullah · Tafazzal Hossain · Chang-Sik Ha

Received: 1 March 2011 / Accepted: 28 May 2011 / Published online: 14 June 2011

Abstract The growth kinetics, isotropic-to-anisotropic transformation, structural properties and surface morphology of polyvinylpyrrolidone (PVP)-coordinated gold nanoparticles are reported in this work. The reduction of gold ions, kinetics, and growth mechanism of gold nanoparticles, and the coordination between PVP and gold are explored for the first time in this single report. The layer-by-layer growth mechanism (adsorption of gold ions to the nuclei and their subsequent reduction) was observed in the growth of isotropic nanoparticles during the initial stage of the reaction, whereas the Ostwald ripening mechanism (growth of larger particles at the expense of smaller particles) was observed in the growth of the anisotropic nanoparticles in the later stage of the reaction. The surface plasmon resonance band for the anisotropic nanoparticles (average size for a typical sample was ca. 9 nm) was blue-shifted (20 nm) toward that of the isotropic nanoparticles (whose average size is much smaller than that of the anisotropic nanoparticles). The increased effective electron density on the surface of anisotropic particles was the cause of this blue shift. The resultant gold colloids were very stable because the PVP molecules were coordinated through both the C–N and C=O groups, instead of the C=O group alone. The positions of the surface plasmon band and morphology of the gold products were strongly dependent on the amount of PVP.

Md. Habib Ullah · C.-S. Ha (✉)
Pioneer Research Center for Nanogrid Materials, Department of Polymer Science and Engineering, Pusan National University, Busan 609-735, Korea
e-mail: csha@pnu.edu

Md. Habib Ullah · T. Hossain
Department of Physics, School of Natural Science, American International University-Bangladesh, Banani, Dhaka 1213, Bangladesh

Introduction

Colloids of noble metal nanoparticles exhibit a strong optical resonance phenomenon that is absent in the bulk phase. The surface plasmon resonance is the coherent excitation of all of the 'free' electrons within the conduction band, leading to an in-phase oscillation [1]. For very small particles less than 2 nm in size, the plasmon oscillation is strongly damped and exhibits a monotonically increasing absorbance toward higher energies [1–3]. This is because the electron density in the conduction band becomes very small. For larger particles whose size is still small compared with the wavelength of light, excitations of the surface resonance can take place in visible light and give rise to a characteristic surface plasmon band [1]. The plasmon band of a specific metal is sensitive to the nanoparticle size, shape, local dielectric environment, and interparticle gap [1–16]. In addition to their role in optical resonance, metal (e.g., silver, gold, and platinum) nanoparticles play important roles in many different areas, such as electronics, catalysis, information storage, and surface-enhanced Raman scattering (SERS) applications.

Gold is an important noble metal. Gold nanoparticles are a promising candidate for biomedical applications, such as drug delivery, biodetection, and biolabeling, which require nanoparticles that are nontoxic and highly soluble in water as well as in physiological solutions [17–21]. The size distribution of gold nanoparticles is considered to be important for their biomedical applications. The size-dependent cytotoxicity of gold nanoparticles was recently studied by Pan et al. [22]. They reported that very small gold compounds and

large ($\sim$15 nm) gold colloids were comparatively nontoxic, whereas particles 1–2 nm in size were highly toxic. The most important requirement for colloidal nanoparticles is a protective agent that keeps the particles from aggregating and makes them functional in soluble media. In many synthetic approaches, poly(vinylpyrrolidone) (PVP) has been frequently used as a protecting polymer [23–29]. PVP contains a long and soft polyvinyl backbone, and its individual monomer contains an amide group. These structural features make PVP an ideal stabilizing agent for transition metal particles, especially for noble metal particles. One of the most important features of this polymer is that it is a completely nontoxic, water-soluble polymer used for gene delivery to muscle tissue [30]. Currently, PVP is most commonly used to direct anisotropic metal growth by selectively absorbing on specific metal crystallographic planes by well-known methods including microwave-assisted polyol methods that are performed at relatively high reaction temperatures (over 150 °C) [11, 25, 27, 31, 32]. Only a few papers have been published regarding the growth of particles and their coordination to PVP at a relatively low reaction temperature. However, the growth of metal particles and their interaction with PVP depend on the synthesis conditions, such as solvent, reduction process, temperature, and concentrations of precursor elements. Due to these considerations, the morphologies of PVP-stabilized particles and their growth kinetics are quite variable [33–36]. Unlike spherical nanoparticles, anisotropic nanoparticles often possess different atomic planes and/or increased surface area. Particles with larger surface areas contain more exposed atoms and hence more electrons on their surfaces. To the best of our knowledge, however, the growth morphology of these particles and their optical properties in an aqueous system at room temperature have not been reported.

We investigated the growth kinetics and isotropic-to-anisotropic transformation of gold nanoparticles stabilized with PVP through double coordination. The anisotropic gold nanoparticles are completely water-soluble, and the morphology of the resultant gold products is independent of the growth time. The structural properties and surface morphology of PVP–gold nanoparticles were observed. The optical responses to the gold colloids prepared with various molar concentrations of PVP with respect to the gold salt are also studied in this work.

Experimental

Materials

Gold(III) chloride trihydrate [($HAuCl_4 \cdot 3H_2O$), purity $\geq$99.9%], poly(vinylpyrrolidone) (average $M_w \sim 29{,}000$), and sodium borohydride were purchased from Aldrich. All chemicals were used as received. Deionized water (aqua-MAX) was used throughout the experiments to avoid any impurities such as organic, ionic, and bacterial compounds.

Preparation of gold colloids

In a typical synthesis, 1 mL of aqueous $HAuCl_4 \cdot 3H_2O$ (61.5 mM) was added to 5 mL of a clear aqueous solution of PVP (4.44 g, 0.1531 mmol) under magnetic stirring at room temperature (27–30 °C). The solution mixture was stirred for an hour to make a homogeneous PVP–Au^{3+} solution. The Au^{3+} ions in the composite were reduced by adding $NaBH_4$ solution (30 μL, 0.4 M). The solution was stirred for 16 h to obtain a stable gold colloid. The colloids were diluted (50–100 times) with deionized water for kinetic, optical, and TEM studies.

Characterization

The absorption spectra were recorded in a quartz cell with an optical path length of 1 cm using a Hitachi U-2010 spectrometer. The colloids were diluted equally such that the molar concentration was held constant. TEM studies were performed using a JEOL-JEM 2010 electron microscope operating at 200 kV. For the X-ray diffraction (XRD), X-ray photoelectron spectroscopy (XPS), and Fourier-transform infrared spectroscopy (FTIR) measurements, the colloidal nanoparticles were transformed into powder samples by spreading the colloids onto glass substrates and drying them in an oven at 30 °C for approximately 3 days. Prior to drying them for the XRD, XPS, and FTIR studies, the colloidal solutions were treated with a chloroform solution (30 mL) containing tetraoctylammonium bromide (0.2 g). Three milliliters of colloidal gold was added to 30 mL of the chloroform solution and stirred vigorously for a few hours to remove the unbonded gold and PVP from the solution. The top water phase was collected after the chloroform solution had settled. The XRD data were collected on a Rigaku Minifex X-ray diffractometer operating at 40 kV and 30 mA using Cu K_α ($\lambda = 1.5401$ Å) radiation. XPS was conducted using a VG-Scientific ESCA lab 250 spectrometer; Al K_α radiation at 1486.6 eV was used, and the peak positions were referenced internally to the C 1s peak at 284.6 eV. The FTIR spectra were recorded at room temperature on a JASCO Corp. FT/IR-430 spectrometer.

Results and discussion

Scheme 1 illustrates the preparation of stable gold nanoparticles via a simple green synthetic pathway. First, Au^{3+} ions were adsorbed onto PVP, and the composite ions were

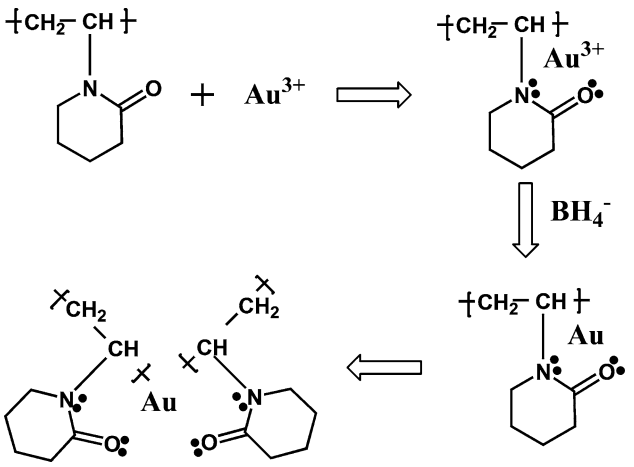

Scheme 1 Schematic illustration of preparation of PVP-coordinated gold nanoparticles

reduced with BH_4^- to yield PVP-enchained Au(0). The electronic absorption spectra of the gold ion solution and PVP adsorbed gold ion solution were clearly distinguishable (Fig. 1). For the $[AuCl_4]^-$ solution, we observed a sharp absorption band at 287 nm with a long tail that is attributed to the ligand-to-metal charge transfer transition of the $Au^{3+}Cl_4^-$ ions. The position of the absorption band (~304 nm) of the PVP–Au^{3+} composite sol is shifted to a lower frequency (higher wavelength), and the band is broader in shape compared to that of the ionic solution of gold only. This indicates that the cationic gold is electrostatically stabilized with the lone pair electrons of oxygen in the carbonyl group and/or nitrogen in the pyrrolidone ring of the PVP molecule, as shown in Scheme 1. After the $NaBH_4$-mediated reduction of the ionic composite, the spectra dramatically changed with time (Fig. 2a). After 3 min, a broad shoulder appeared in the range of

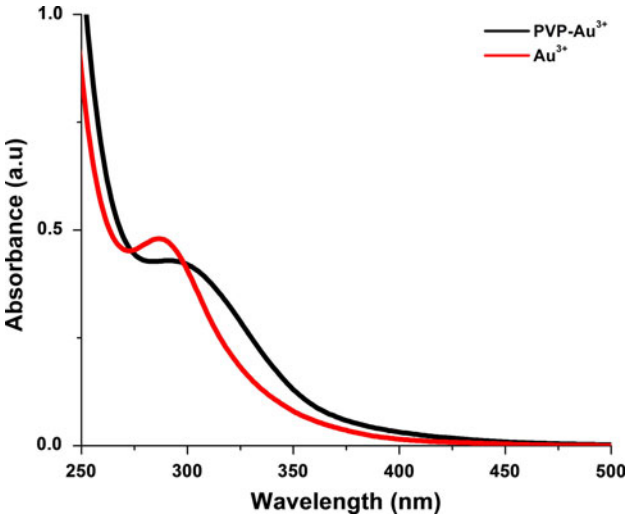

Fig. 1 UV–Vis absorption spectra of Au^{3+} and PVP–Au^{3+} ions

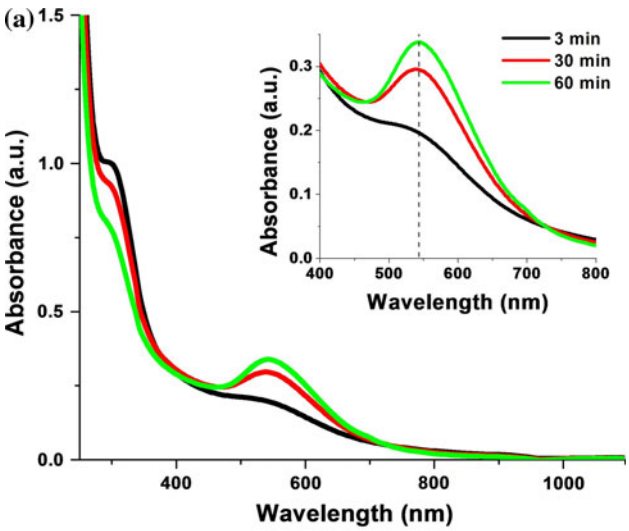

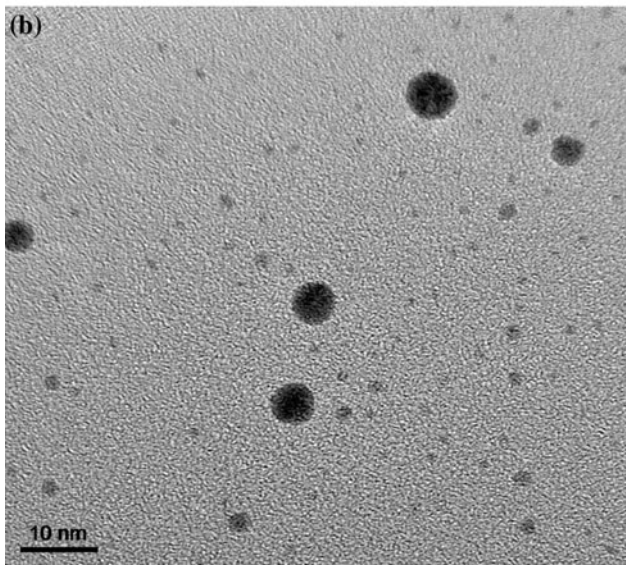

Fig. 2 **a** UV–Vis–NIR absorption spectra at different times after the start of reduction. The spectra show that the growth proceeds at the expense of the ionic phase. The *inset* shows the plasmon band region of these spectra. **b** HRTEM image of PVP–gold sol 60 min (S1) after the start of the reduction. The image shows non-agglomerated isotropic particles with a broad size distribution (~0.5–2.0 nm and ~4–5.5 nm)

490–650 nm with the respective change in the shape of the ionic band. This low intensity shoulder-like band in the visible range was recognized as the plasmon band of the small Au(0) clusters with a broad size distribution [2, 37]. The presence of the ionic band and trace of the plasmon band indicate that the reduction reaction and particle growth take place simultaneously. Thirty minutes after the start of the reduction reaction, the shoulder appears as a broad band centered at 545 nm, which becomes comparatively more intense as the reaction time increases to 1 h (inset of Fig. 2a). The ionic band tends to diminish with time (as shown in Fig. 2a). We investigated the dimensions of the

gold particles of sol S1 (S1 prepared after undergoing a reduction reaction for 60 min) by using a high-resolution transmission electron microscope (HRTEM) having a point-to-point resolution of 0.19 nm. A drop from each diluted aqueous sol of S1 was placed on a copper TEM grid completely covered with carbon, and the water was then left to evaporate. Images of the product were recorded using a digital charge-coupled device (CCD) camera attached to the TEM. The HRTEM image (Fig. 2b) of S1 reveals non-agglomerated isotropic (spherical) gold nanoparticles of different sizes (~0.5–2.0 and ~4–5.5 nm). Our result is consistent with the result obtained by Kemal et al. [38]. They found 2–3 nm PVP–gold particles by TEM analysis, through which they observed a UV–Vis absorption band at ~545 nm. From the above findings, however, it may be concluded that three different chemical potentials [39, 40] co-exist after adding $NaBH_4$ to the ionic sol. The coexisting chemical potentials are due to the ionic composites, nuclei (very small particles of gold formed immediately after reduction) and comparatively larger particles. The non-colliding nature of the particles on the TEM grid and gradual loss of ionic band structure on the absorption spectra reveal that the larger particles do not grow at the expense of the comparatively smaller particles. The growth of the particles should follow the layer-by-layer growth mechanism, i.e., the gradual adsorption of ions onto the surface of the nuclei followed by the reduction of the ionic layer [41].

The gold sol was stirred for another 15 h and then subjected to microscopic and spectroscopic investigations. The HRTEM image of the diluted gold sol S2 (S2 prepared after undergoing a reduction reaction for 16 h) showed the mostly anisotropic morphology of the particles dispersed well on the carbon-coated copper grid (Fig. 3a). The particles viewed on the TEM grid exhibited a variety of shapes, such as triangular (prismatic), octahedral, spherical, and cubic shapes. The dimensions of the particles were distributed over the range of 7–12 nm with an average size of 9 nm. The UV–Vis–NIR spectrum of S2 shows a strong plasmon band at 525 nm without any long tail (Fig. 3c, solid line). The complete disappearance of the ionic band in the spectrum indicates the existence of metal particles only. However, the 20 nm blue shift (from 545 to 525 nm) of the plasmon band with increasing size could not be explained by Mie theory [42]. According to Mie theory, the absorption maximum shifts towards longer wavelengths (red shifts) as the average particle size (homogeneous and isotropic) becomes larger. Such a blue shift with increasing reaction time was, however, previously observed by Esumi et al. [43] and Chow and Zukoski [44], although the causes of the blue shifts were consistent with Mie theory. They reported that although in the initial stage of the reaction large fluffy particles, which appear to be composed of

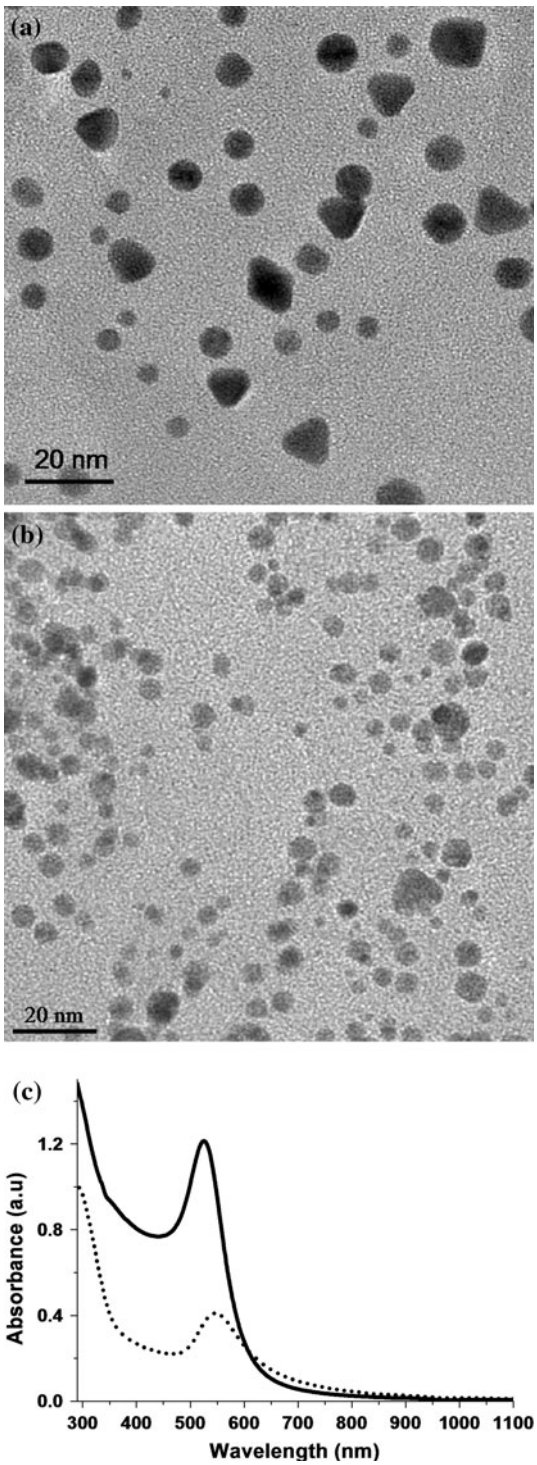

Fig. 3 **a** The HRTEM image of the corresponding sol of S2 showing mostly anisotropic particles with a size range of 7–12 nm; average size is 9 nm. **b** HRTEM image exploring the evolution of anisotropic particles (ca. 7 nm) from isotropic particles. The image was taken from the PVP–gold sol 4 h (S3) after the reduction started. **c** UV–Vis–NIR absorption spectrum (*solid line*) of PVP–gold sol 16 h (S2) after the reduction started. The strong plasmon band that appeared at 525 nm is stable and is blue-shifted by 25 nm with respect to the plasmon band that appeared at S1; The *dotted line* denotes the absorption spectrum of S3. The maximum intensity of the plasmon band appears at 532 nm with a long tail

smaller particles, are formed, the large agglomerate falls apart, giving rise to a continual increase in the number density of small particles as the reaction proceeds. In our case, we did not observe such an agglomeration in the initial stage of reaction, but rather, monodispersed particles were observed on the TEM grid (Fig. 2). Therefore, for the blue shift of the plasmon band with increased intensity, the effects such as the shape of the gold particles, the dielectric contribution of the surrounding polymer to the gold core, and free electron density (depending on size, shape, and surface interaction between the metal and polymer) become more prominent compared to the Mie scattering effect as the average particle size increases [1, 15, 45, 46]. The relationship between the surface plasmon resonance frequency (ω_0) and the electron density (n) in the metal can be written as [45],

$$\omega_0^2 = \frac{ne^2}{\varepsilon_0 m_e(\varepsilon_\infty + \kappa\varepsilon_m)}$$

where ε_∞ is the dielectric contribution due to the atomic core polarizability, e is the electronic charge, m_e is the effective mass of an electron, ε_0 is the vacuum permittivity, κ is a screening parameter related to the shape of the nanoparticles, and ε_m is the dielectric constant of the surrounding medium. It was reported that the plasmon band shift increases linearly with the change in the refractive index of the surrounding environment of the metal core [45, 47], where the refractive index (n) is related to the ε_m of the medium by $\varepsilon_m = n^2$ for high frequencies. According to their linear correlation plot between n and the plasmon peak position (λ_{max}), for $\Delta n = 0.1$, a 13-nm change in wavelength is observed. Thus, for 25-nm blue shift in our work, the magnitude of the refractive index is $\Delta n \approx 0.2$. The blue shift in this work was, however, not only for the change in the refractive index due to the surrounding environment but also for the increase in electron density. It is important to note that PVP in an aqueous environment reorganizes itself into a complex network of polymer backbones stabilized by electrostatic interactions. During the formation of the anisotropic particles, the conformation of the polymer and the interaction between the polymer and the gold might be changed. Thus, the surface environment of the gold particles is also changed. Consequently, the effective electron density may increase significantly so as to shift the plasmon resonance to a higher frequency, i.e., the shift of the absorption maximum to a shorter wavelength. It is well established for polymers in solution that the change in the refractive index is proportional to the concentration. Thus, if the solution concentration is reduced, the refractive index is also reduced. It should be also noted that a blue shift of approximately 130–150 nm is observed when the solution refractive index is reduced by only 1 [45, 48].

The isotropic-to-anisotropic morphology transformation of gold particles with elapsed time was investigated by examining the morphological and optical data of S3 (S3 prepared after undergoing the reduction reaction for 240 min). Figure 3b shows an HRTEM image of a drop of the gold sol S3. The image shows how the gold particles collide with each other to grow into anisotropic particles. Hence, the growth kinetics of S3 is different from that of S1. The average size (ca. 7 nm) of the particles of S3 is larger than that of the particles of S1 but smaller than that of S2.

To clarify whether the ionic phase still exists or not and to verify the nature of the particles observed on the TEM grid, we obtained the absorption spectrum of S3. The absorption spectrum (Fig. 3c, dotted line) provided evidence that the sol no longer contains the ionic phase of gold. The long-tailed broad absorption band supports the TEM observation. Although the average particle size is larger than that observed for S1, a 13-nm blue shift was observed. Such a blue shift may arise from the reasons described above.

The formation mechanism of anisotropic particles based on TEM imaging is illustrated in Scheme 2. In general, the average size of the particles increases with time, and the number of second-phase particles (smaller particles) must decrease with time. Thus, the change in morphology occurs as a result of the dissolution of the small particles and the transfer of their mass to the larger particles. The driving force of this process is the decrease in the total surface free energy. The total interfacial area of the system must decrease with time for the system to attain thermodynamic

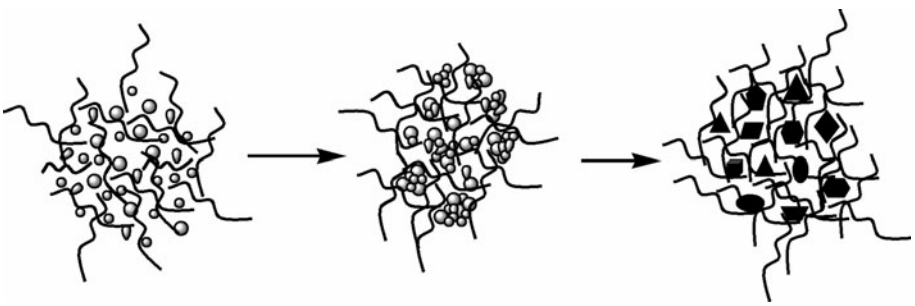

Scheme 2 Schematic view of isotropic-to-anisotropic transformation

equilibrium. This interfacial area reduction process is known as Ostwald ripening [49, 50]. Recently, Rocha et al. [51] reported that anisotropic nanoparticles can grow preferentially over spherical ones due to the fact that energy required to build larger anisotropic structures could be less than that required to build isotropic structures. This is resemblance to our Scheme 2. However, the development of a suitable quantitative method to better understanding the growth of anisotropic nanoparticles is still a challenging task.

To determine the relationship between the formation of gold particles and the reaction time, the evolution of the optical density (absorbance) at 525 nm was monitored and is presented in Fig. 4. It is apparent from the time versus absorbance curve that polynomial growth of the gold nanoparticles occurred until a stable state was reached. In the time window of 0–30 min, the optical density increases rapidly, indicating faster nucleation and growth. After 30 min, the absorbance increases slowly and at nearly the same rate until approximately 120 min of reaction time. This indicates that the growth rate is slower than that observed during the first 30 min. This may happen because the concentration of gold ions decreases with increasing time. After a reaction time of 120 min, the absorbance increases more slowly up to ca. 200 min. This may be due to the nearly complete relaxation time for the growth of the isotropic particles. In the time window of ~205–330 min, the parabolic increase in absorbance with time is corroborated by TEM observation (Fig. 3b) for S3. A large shoulder-like absorbance is observed at longer times (until the stable state is reached). This supports the hypothesis illustrated by Scheme 2, where the unstable colliding particles are slowly transformed into smooth anisotropic particles corresponding to the stable state.

Because the UV–Vis absorption spectra have been proven to be quite sensitive to the formation and morphology of metal colloids [15, 52], we studied the effect of the PVP concentration on the final gold colloids. Figure 5a compares the absorption bands (i.e., surface plasmon resonance bands) of PVP–gold nanoparticles obtained at five different PVP concentrations. The resonance peak positions are tunable according to the PVP/Au^{3+} mole ratio (where the Au^{3+} concentrations were kept constant). Red shifts are observed in the peak positions of the surface plasmon resonance bands with decreasing PVP concentration. The peak widths are also broadened with decreasing PVP concentration. The red shifts and broadening of the peak widths indicate the increase in particle size. In the absence of PVP, a very broad shoulder-like plasmon band (half width at maximum of 630 nm) was observed (Fig. 5b). The broad absorption band with a long tail indicates the presence of large aggregations of small particles because the absorption spectra of collective particles

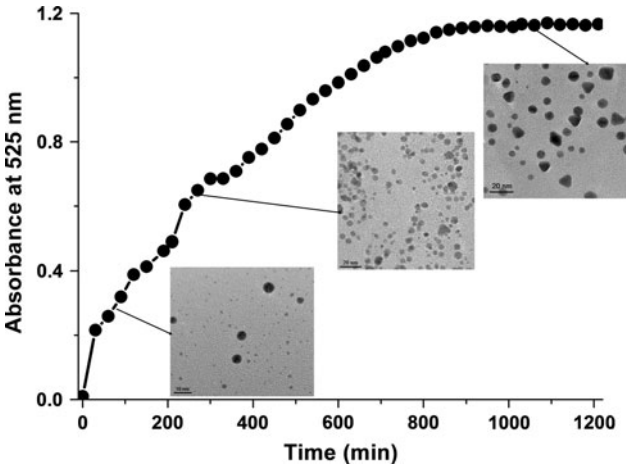

Fig. 4 Change in the absorbance of the PVP–gold sol at 525 nm as a function of the elapsed time at room temperature (ca. 27 °C). The time–absorbance curve shows polynomial growth. The major stages of the growth process are marked by the TEM images

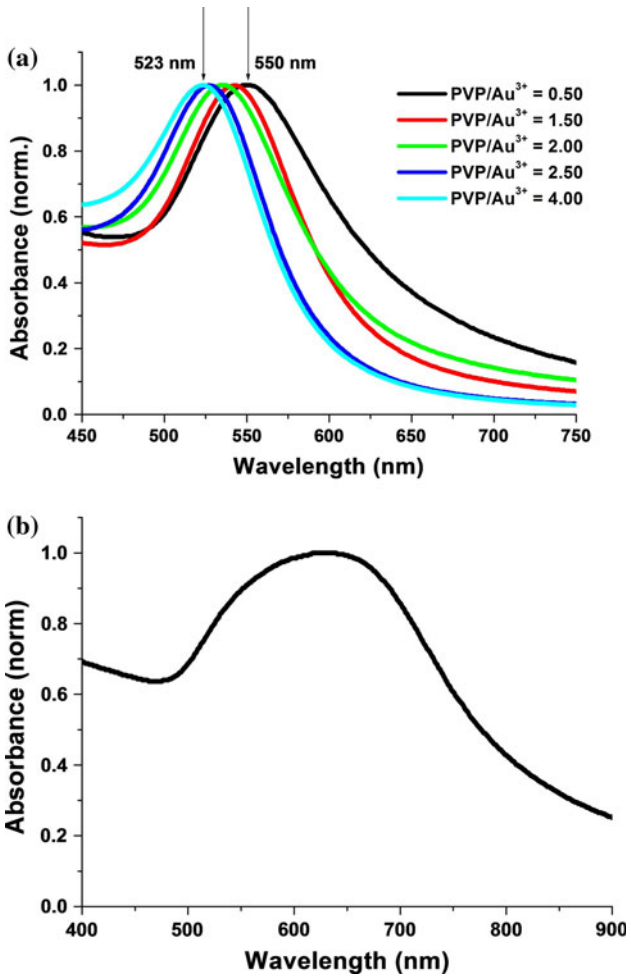

Fig. 5 The absorption spectra of PVP–gold sols with various amounts of PVP (*top*). The absorption spectrum of the gold sol in the absence of PVP (*bottom*)

are flatter and broader and their maxima appear at longer wavelengths than those of isolated particles [12, 53]. This might be due to multiple polarization or dipole–dipole interactions [52]. Furthermore, dipolar scattering and Rayleigh scattering play important roles in aggregated particles or large particles (typically >25 nm) and are accompanied by a significant broadening of the absorption peak [52, 54]. To corroborate the absorption spectra obtained for the gold colloids with various PVP contents, we took TEM micrographs of two typical samples. Figure 6a shows a TEM image of a gold colloid with a PVP/Au^{3+} mole ratio of 2. The image shows non-aggregated anisotropic particles with an average size distribution of 16 nm, which is 7 nm larger than that obtained for a gold colloid with a PVP/Au^{3+} mole ratio of 3. In the absence of PVP, the TEM grid is covered with aggregated gold particles (Fig. 6b), which is remarkably consistent with their absorption spectrum (Fig. 5b). In addition to the time resolved absorbance (as shown in Fig. 4) observed during the growth process and stable state, we studied the stability of a typical gold colloid beyond the synthesis period. Figure 7 compares the absorption spectra of an as-synthesized PVP–gold colloid to that of the same colloid 3 months after synthesis. The plasmon band of the aged colloid did not shift with respect to that of the as-synthesized one. The result indicates that the particle morphology of the final products remains nearly unchanged over time. Moreover, this phenomenon reveals that the stability of the colloid is due to the strong coordination of PVP to the gold surface, instead of the adsorption of PVP to gold.

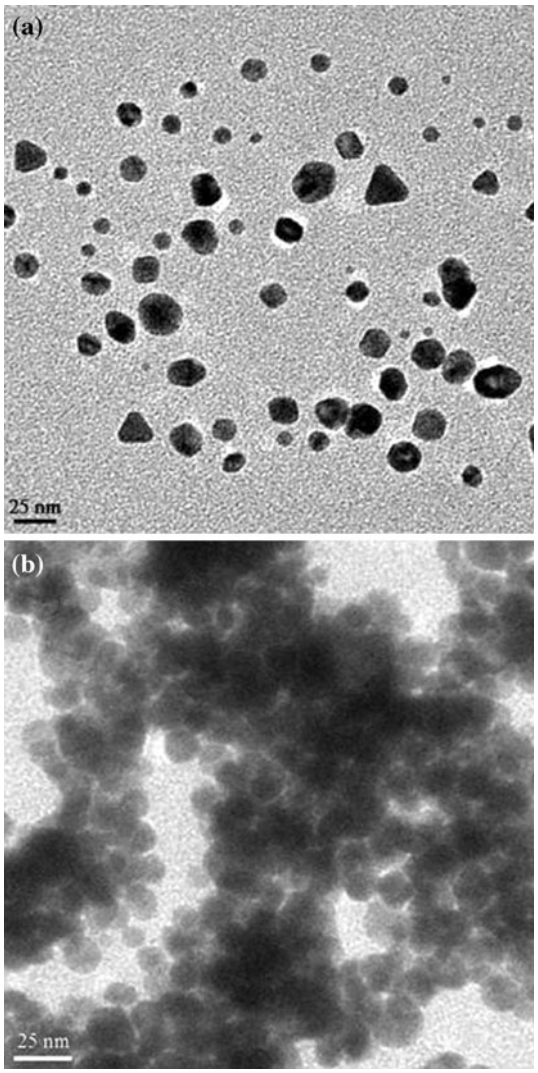

Fig. 6 Effect of PVP concentrations on morphology. **a** TEM image of PVP–gold sol when PVP/Au^{3+} mole ratio was kept at 2. The image shows non-agglomerated anisotropic particles with an average size of 16 nm, which is 7 nm larger than the particles obtained when the PVP/Au^{3+} mole ratio was kept at 3. **b** TEM image of the gold sol in the absence of PVP. The image shows very large aggregations

To investigate the structural morphology of the core/shell (gold/PVP) materials, we used XRD, electron diffraction (ED), and FTIR absorption spectroscopy. The XRD pattern of a typical product (PVP/gold = 2) shows the fingerprints of PVP and gold (Fig. 8a). The broad peaks at $2\theta = 9°–15°$ and $2\theta = 19°–25°$ are associated with the amorphous nature of PVP with a small fraction of crystalline phases, as reported previously [26]. The diffraction peaks corresponding to the (111), (200), (220), (311), and (222) planes correspond to the face-centered-cubic (fcc) structure of gold. The ED pattern (inset of Fig. 8a) of the corresponding product on the TEM grid agrees with the XRD pattern of the gold phase [55]. This indicates that the product is composed of pure crystalline gold and PVP, which may exist together while interacting with each other via covalent-type bonds [56]. The FTIR spectra of pure PVP and PVP–gold are presented in Fig. 8b. Pure PVP displays some typical bond absorptions at approximately

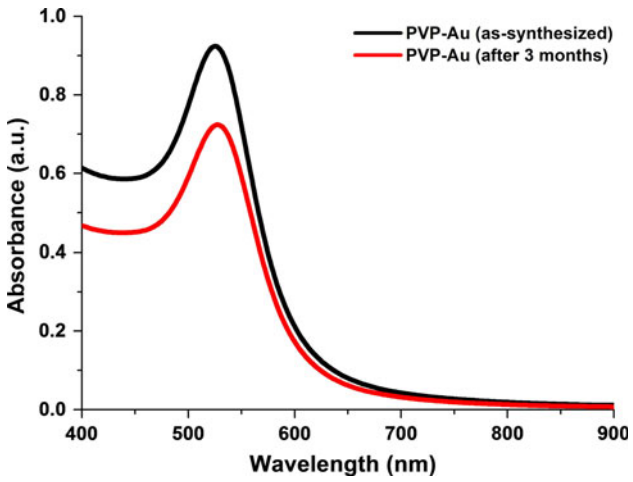

Fig. 7 Visible–NIR absorption spectrum of the as-synthesized PVP–gold sol compared with the spectrum of a similar sol after 3 months of aging

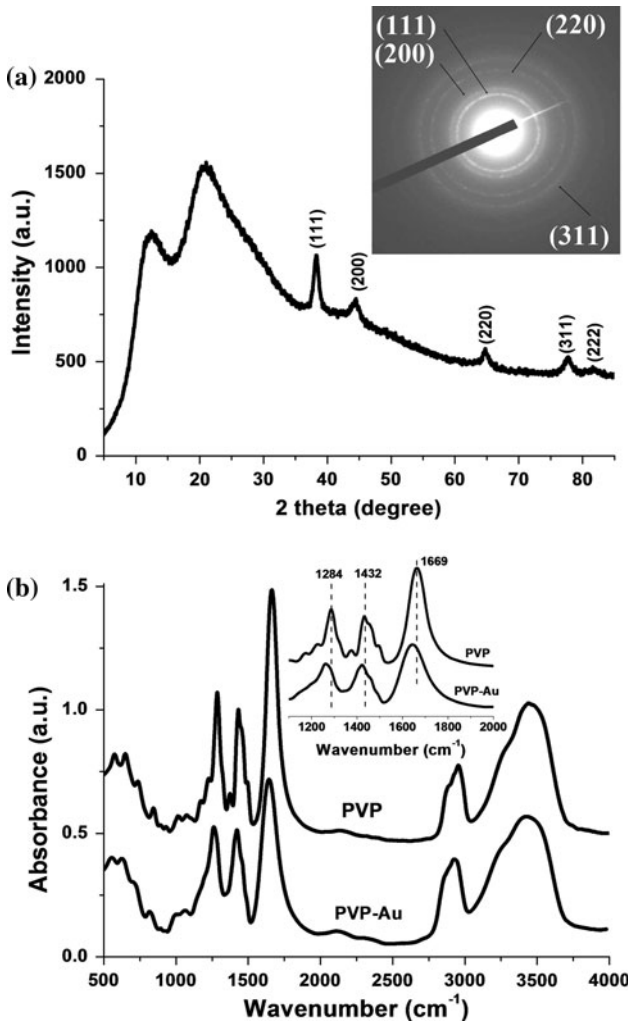

Fig. 8 **a** X-ray diffraction pattern of typical anisotropic PVP–gold nanoparticles. The pattern shows the existence of PVP along with face-centered-cubic (fcc) gold. The *inset* shows the electron diffraction (ED) pattern of the product. The ED pattern confirms the fcc structure. **b** FTIR spectra of PVP and PVP–gold nanoparticles. The *inset* shows the magnified part of a particular region

1284, 1432, 1669, 2930, and 3440 cm^{-1} arising from the absorptions of the N → H–O complex, the pyrrolidone ring, and the bond vibrations from the C=O, C–H, and O–H (from water impurities) moieties, respectively [8]. Compared to the spectrum of pure PVP, that of PVP–gold shows that the position and intensity of the band related to the C–H bonds varies very little because the hydrocarbon chain is inert to gold. However, the ratio of the intensities of $\nu_{(N \rightarrow O-H)}$, $\nu_{(pyrrolidone\ ring)}$, and $\nu_{(C=O)}$ to $\nu_{(C-H)}$ are remarkably reduced in PVP–gold compared to that of pure PVP. Moreover, the bands arising from these vibrational groups become wider and are further red-shifted to 1260, 1421, and 1637 cm^{-1}, respectively. These reductions in wavenumbers may result from the bond-weakening that arises from the partial donation of the O/N lone-pair electrons of PVP to vacant orbitals on the gold surface [11, 57, 58].

To better understand the interaction between PVP and the gold surface and the surface state of gold, XPS studies were conducted. Because the hydrocarbon groups of the PVP molecules are ideally inert toward the gold surface, we studied the high-resolution nitrogen and oxygen spectra of both PVP and PVP–gold. Figure 9a and b shows the spectra for N 1s and O 1s, respectively, obtained from PVP alone, and Fig. 9c and d shows those obtained from PVP–gold. The N 1s peak, for PVP and PVP–gold could be resolved into two peaks. For PVP, the deconvoluted peaks at 397.9 and 399.3 eV can be assigned to polar nitrogen and nitrogen in the carbon environment, respectively. For PVP–gold, the shape and position of the N 1s peak are different (Fig. 9c). The deconvoluted peaks are shifted to higher binding energies of 398.4 and 400 eV, respectively. This result indicates that the overall chemical environment surrounding nitrogen is altered due to the interaction between nitrogen and the surfaces of the gold nanoparticles. Similarly, the O 1s peak for PVP could be resolved into two peaks at 529.2 and 530.2 eV (Fig. 9b). These states can be assigned to polar oxygen and oxygen in the carbonyl environment, respectively. For PVP–gold, similar to the N 1s peak, the shape and position of the O 1s peak are altered compared to those observed for pure PVP. The resolved peaks are shifted to 530.3 and 530.8 eV, respectively, indicating the existence of an interaction between oxygen and the gold surface. The shifts of the N 1s and O 1s peaks to higher binding energies can be attributed to the decrease in the electron density of the nitrogen and oxygen atoms [59] because PVP coordinates with gold through the C–N in the pyrrolidone rings and C=O in the carbonyl groups, as corroborated by the FTIR analyses. Figure 9e shows the core level spectrum of Au 4f. The spectrum shows that the signal-to-noise ratio is low. A low signal appeared because it was not possible to etch the sample (PVP–gold powder described in "Experimental" section) with ion-beam irradiation. However, using curve-fitting software, the corresponding peaks could be resolved. The two peaks at 83.8 and 87.5 eV are attributed to $4f_{7/2}$ and $4f_{5/2}$, respectively, from Au(0). These peaks, however, shift toward a low binding energy relative to the bulk gold atoms (84.0 eV for Au $4f_{7/2}$ and 87.7 eV for Au $4f_{5/2}$) [60]. Generally, the Au 4f core-level energy is very sensitive to the surrounding chemical environment of the gold core, particularly to the electron-donating ability of the polymeric or organic ligands and the strength of the interaction between gold and the polymeric or organic ligands. This shift may reveal that electrons are inclined to transfer from the oxygen and nitrogen of PVP to the gold interface, implying that there is a strong interaction between the electrons [61].

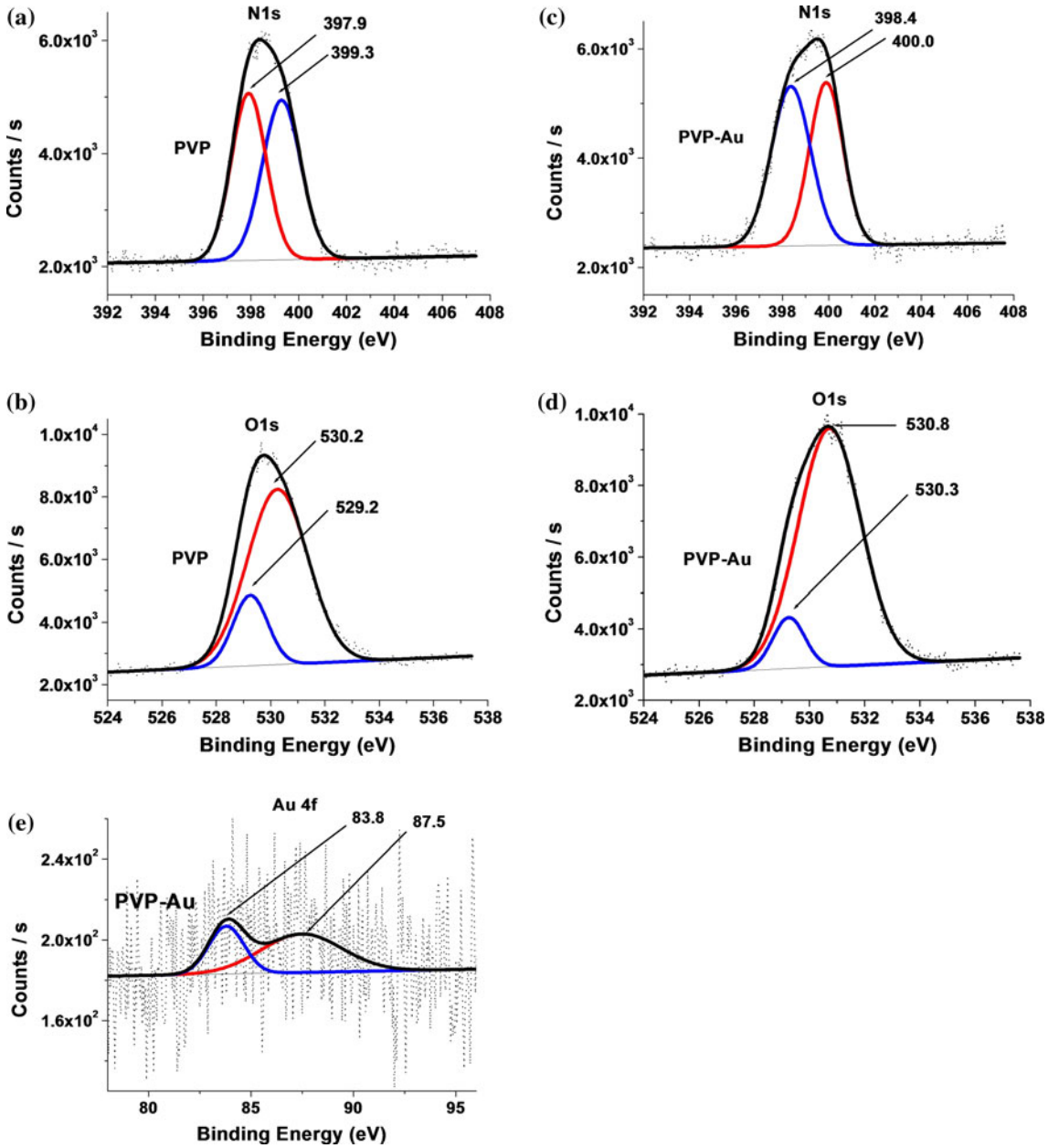

Fig. 9 High resolution XPS spectra of **a** N 1s, **b** O 1s of PVP, and **c** N 1s, **d** O 1s, and **e** Au 4f of PVP–gold nanoparticles

In addition to the increased surface electron density of gold due to its anisotropic shape, the tendency of electrons in PVP to move toward the gold surface could greatly increase the effective surface electron density of anisotropic gold nanoparticles. According to the relationship between the plasmon frequency and effective electron density described earlier, a blue shift was observed instead of a red-shift for large anisotropic particles. In this way, we can conclude that PVP molecules were coordinated to gold through both the C–N and C=O groups instead of the C=O group alone.

Conclusions

In summary, we have investigated the formation of isotropic and anisotropic gold nanoparticles stabilized with PVP. The growth kinetics and tuning of morphologies (isotropic to anisotropic) are described based on the optical and microscopic results. The results indicate the polynomial growth of gold nanoparticles. The structural morphology of the core/shell (gold/PVP) particles was analyzed by XRD, FTIR, and XPS. The FTIR and XPS studies showed that the gold particles are doubly

coordinated through C–N and C=O groups, instead of through the C=O group alone. These well-coordinated gold nanoparticles are highly stable such that the morphology of the gold colloids does not change over time. The significant effects of PVP on the gold particles, however, could be observed by optical absorption and TEM.

Acknowledgements This work was supported by the National Research Foundation of Korea (NRF) Grant funded by the Ministry of Education, Science and Technology, Korea (MEST) (Acceleration Research Program (No. 2011-0000385) and the Pioneer Research Center Program (No. 2011-0001667/2011-0001668), a grant from the Fundamental R&D program for Core Technology of Materials funded by the Ministry of Knowledge Economy, Korea, and the MEST for the Brain Korea 21 Project. We thank the Korea Basic Science Institute for the TEM and XPS measurements.

References

1. Link S, El-Sayed MA (2000) Int Rev Phys Chem 19:409
2. Wilson OM, Scott RWJ, Garcia-Martinez JC, Crooks RM (2005) J Am Chem Soc 127:1015
3. Ullah MH, Kim I (2006) J Nanosci Nanotechnol 6:1
4. Lazarides AA, Schatz GC (2000) J Phys Chem B 104:460
5. Zhao L, Kelly KL, Schatz GC (2003) J Phys Chem B 107:7343
6. Malinsky MD, Kelly KL, Schatz GC, Duyne RPV (2001) J Am Chem Soc 123:1471
7. Xue C, Millstone JE, Li S, Mirkin CA (2007) Angew Chem Int Ed 46:8436
8. Métraux GS, Cao YC, Jin R, Mirkin CA (2003) Nano Lett 3:519
9. Wiley BJ, Im SH, Li ZY, McLellan J, Siekkinen A, Xia Y (2006) J Phys Chem B 110:15666
10. Orendorff CJ, Sau TK, Murphy CJ (2006) Small 2:636
11. Zhang J, Liu H, Wang Z, Ming M (2007) Adv Funct Mater 17: 3295
12. Ullah MH, Chung W-S, Kim I, Ha CS (2006) Small 2:870
13. Ullah MH, Kim I, Ha CS (2006) Mater Lett 60:1496
14. Gulati A, Liao H, Hafner JH (2006) J Phys Chem B 110:22323
15. Chen CF, Tzeng SD, Chen HY, Lin KJ, Gwo S (2008) J Am Chem Soc 130:824
16. Jain PK, Huang W, El-Sayed MA (2007) Nano Lett 7:2080
17. Liu GL, Yin Y, Kunchakarra S, Mukherjee B, Gerion D, Jett SD, Bear DG, Gray JW, Alivisatos AP, Lee LP, Chen FF (2006) Nat Nanotechnol 1:47
18. Lee JS, Han MS, Mirkin CA (2007) Angew Chem Int Ed 46:4093
19. Chen J, Wiley B, Li ZY, Campbell D, Saeki F, Cang H, Au L, Lee J, Li X, Xia Y (2005) Adv Mater 17:2255
20. McKenzie F, Faulds K, Graham D (2007) Small 3:1866
21. Shi X, Wang S, Meshinchi S, Antwerp MEV, Bi X, Lee I, Baker JR (2007) Small 3:1245
22. Pan Y, Neuss S, Leifert A, Fischler M, Wen F, Simon U, Schmid G, Brandau W, Jahnen-Dechent W (2007) Small 3:1941
23. Hirai H, Yakura N (2001) Polym Adv Technol 12:724
24. Ma H, Huang S, Feng X, Zhang X, Tian F, Yong F, Pan W, Wang Y, Chen S (2006) Chem Phys Chem 7:333
25. Ullah MH, Kim JH, Ha CS (2008) Mater Lett 62:2249
26. Teranishi T, Kiyokawa I, Miyake M (1998) Adv Mater 10:596
27. Harpeness R, Peng Z, Liu X, Pol VG, Koltypin Y, Gedanken A (2005) J Colloid Interface Sci 287:678
28. Sun L, Liu A, Tao X, Zhao Y (2011) J Mater Sci 46:839. doi: 10.1007/s10853-010-4826-4
29. Liu D, Ren S, Wu H, Zhang Q, Wen L (2008) J Mater Sci 43:1974. doi:10.1007/s10853-008-2459-7
30. Blezinger P, Wang J, Gondo M, Quezada A, Mehrens D, French AS, Sullivan S, Rolland A, Ralston R, Min W (1999) Nat Biotechnol 17:343
31. Sun Y, Yin Y, Mayers BT, Herricks T, Xia Y (2002) Chem Mater 14:4736
32. Zhang F-B, Chen Y, Hu-Lin Li M-W (2006) J Mater Sci 41:2545. doi:10.1007/s10853-006-5332-6
33. Chen J, Saeki F, Wiley BJ, Cang H, Cobb MJ, Li ZY, Au L, Zhang H, Kimmey MB, Li X, Xia Y (2005) Nano Lett 5:473
34. Tsuji M, Hashimoto M, Nishizawa Y, Tsuji T (2003) Chem Lett 32:1114
35. Yamamato M, Kashiwagi Y, Sakata T, Mori H, Nakamoto M (2007) Chem Lett 36:1348
36. Liu Q, Liu H, Zhou Q, Liang Y, Yin G, Xu Z (2006) J Mater Sci 41:3657. doi:10.1007/s10853-006-6199-2
37. Walker CH, St John JV, Wisian-Neilson P (2001) J Am Chem Soc 123:846
38. Kemal L, Jiang XC, Wong K, Yu AB (2008) J Phys Chem C 112:15656
39. Job G, Herrmann F (2006) Eur J Phys 27:353
40. Baierlein R (2001) Am J Phys 69:423
41. Huang ZY, Mills G, Hajek B (1993) J Phys Chem 97:11542
42. Mie G (1908) Ann Phys 25:377
43. Esumi K, Hosoya T, Suzuki A, Torigoe K (2000) Langmuir 16:2978
44. Chow MK, Zukoski CF (1994) J Colloid Interface Sci 165:97
45. Huang W, Qian W, Jain PK, El-Sayed MA (2007) Nano Lett 10:3227
46. Lim IIS, Zhong CJ (2007) Gold Bull 40:59
47. Sönnichsen C, Reinhard BM, Liphardt J, Alivisatos AP (2005) Nat Biotechnol 23:741
48. Link S, El-Sayed MA (1999) J Phys Chem B 103:8410
49. Baldan A (2002) J Mater Sci 37:2171. doi:10.1023/A:1015388912729
50. Wilson GJ, Matijasevich AS, Mitchell DRG, Schulz JC, Will GD (2006) Langmuir 22:2016
51. Rocha TCR, Sato F, Dantas SO, Galvão DS, Zanchet D (2009) J Phys Chem C 113:11976
52. Huang HH, Ni XP, Loy GL, Chew CH, Tan KL, Loh FC, Deng JF, Xu GQ (1996) Langmuir 12:909
53. Jana NR (2005) Small 1:875
54. Michaels AM, Jiang J, Brus L (2000) J Phys Chem B 104:119651
55. Nikoobakht B, Wang ZL, El-Sayed MA (2000) J Phys Chem B 104:8635
56. Zhu J, Shen Y, Xie A, Qiu L, Zhang Q, Zhang S (2007) J Phys Chem C 111:7629
57. Haas I, Shanmugam S, Gedanken A (2006) J Phys Chem B 110: 16947
58. Zhang Z, Zhao B, Hu L (1996) J Solid State Chem 121:105
59. Elechiguerra JL, Larios-Lopez L, Liu C, Garcia-Gutierrez D, Cmacho-Bragado A, Yacaman MJ (2005) Chem Mater 17:6042
60. Handbook of X-ray Photoelectron Spectroscopy, Copyright 1992, 1995 by Physical Electronics, Inc. Eden Prairie, Minnesota 55344, USA
61. Jiang P, Zhou JJ, Li R, Wang ZL, Xie SS (2006) Nanotechnology 17:3533